Title: Dipole relaxation process and giant dielectric permittivity in Eu3+- doped CdMoO4 single crystal

Author: Bogdan Sawicki, E. Tomaszewicz, Tadeusz Groń, M. Berkowski, M. Głowacki, Monika Oboz, Joachim Kusz, Sebastian Pawlus

Citation style: Sawicki Bogdan, Tomaszewicz E., Groń Tadeusz, Berkowski M., Głowacki M., Oboz Monika, Kusz Joachim, Pawlus Sebastian. (2020). Dipole relaxation process and giant dielectric permittivity in Eu3+- doped CdMoO4 single crystal. "Journal of Materiomics" (2020), doi 10.1016/j.jmat.2020.12.010

Journal of Materiomics xxx (xxxx) xxx

Contents lists available at ScienceDirect

Journal of Materiomics

journal homepage: www.journals.elsevier.com/journal-of-materiomics/

Dipole relaxation process and giant dielectric permittivity in Eu^{3+}-doped $CdMoO_4$ single crystal

B. Sawicki [a], E. Tomaszewicz [b, *], T. Groń [a], M. Berkowski [c], M. Głowacki [c], M. Oboz [a], J. Kusz [a], S. Pawlus [a]

[a] A. Chełkowski Institute of Physics, University of Silesia in Katowice, 40-007, Katowice, Poland
[b] Faculty of Chemical Technology and Engineering, Department of Inorganic and Analytical Chemistry, West Pomeranian University of Technology in Szczecin, 71-065, Szczecin, Poland
[c] Institute of Physics, Polish Academy of Sciences, 02-668, Warszawa, Poland

ARTICLE INFO

Article history:
Received 11 September 2020
Received in revised form
28 November 2020
Accepted 18 December 2020
Available online xxx

Keywords:
Scheelite
Single crystal
Solid solution
Paramagnetic behaviour
Relaxation process
Giant dielectric permittivity

ABSTRACT

Single crystal of Eu^{3+}-doped cadmium molybdate ($Cd_{0.9268}\square_{0.0244}Eu_{0.0488}MoO_4$, where $\square$ denotes cationic vacancies) has been successfully grown by the Czochralski method in air and under 1 MPa. X-ray diffraction analysis indicates that as-grown single crystal exhibits tetragonal scheelite-type structure ($a = b = 5.16188(14)$ Å; $c = 11.2080(5)$ Å; space group $I4_1/a$). Eu^{3+} ions do not show long-range order and they are randomly distributed in $CdMoO_4$ framework substituting Cd^{2+} ones. UV–vis diffuse reflectance measurements revealed very close optical band gap (E_g) values, *i.e.* ~1.74 eV along [100] and [001] crystallographic directions that are twice smaller than E_g of microcrystalline pure $CdMoO_4$ as well as powder Eu^{3+}-doped single crystal. Magnetic and electrical studies of Eu^{3+}-doped cadmium molybdate single crystal showed a paramagnetic and *n*-type semiconducting behaviour with the metal-insulator transition above 350 K along both crystallographic directions. Dielectric results analysis using the Cole-Cole fit function revealed that the dipole relaxation process has different time scale depending on the crystallographic direction and exhibits Arrhenius temperature dependence for both studied directions. This fact is accompanied by the colossal dielectric permittivity with $\varepsilon_r > 8 \cdot 10^3$. The above results are considered in the framework of narrow europium multiplets of energy comparable to thermal energy.

1. Introduction

Divalent metal molybdates and tungstates (AXO_4, X = Mo, W) have become subjects of great interest because of various interesting applications in many fields such as photoluminescence [1–8], solid state lasers [9,10] optic fibres [11], microwave dielectrics [12–17], catalysts [18–22] and scintillators [23–28]. Among them, cadmium molybdate is considered as the most interesting material which plays a major role as cryogenic phonon-scintillation detector in the search of neutrinoless double beta decay. $CdMoO_4$ is also a good host for rare-earth ions, exhibiting the emission spectrum thanks to $4f \rightarrow 4f$ transitions [29–31]. Among the rare-earth ions, trivalent europium ones have been very often used as activators in luminescent materials because they show very intense red luminescence related to $^5D_0 \rightarrow {}^7F_1$ and $^5D_0 \rightarrow {}^7F_2$ transitions in the orange and red regions, respectively [29,32–36]. These transitions are strongly dependent upon symmetry as well as local environment of Eu^{3+} whose effect can lead to a wider tuneable colour region. Thus, $CdMoO_4$:Eu^{3+} materials have a potential of showing white light emission due to the red emission from europium ions and blue-green from the host.

Most divalent metal molybdates have scheelite ($I4_1/a$, Z = 4, No. 88) or scheelite-related (*Pnma*, Z = 4, No. 62) structures [5–7,37,38]. In scheelite-type molybdates like $AMoO_4$, where A^{2+} is a metal cation with large ionic radius (A = Ca, Sr, Ba, Cd and Pb, $r_A > 0.90$ Å), Mo^{6+} ions are coordinated to four oxygen ions forming MoO_4 tetrahedra [5–7,37–39]. The materials with tetrahedrally coordinated molybdenum ions have excitation band centered at ~275–330 nm [5–7,29–31]. Each divalent metal cation adopts dodecahedral coordination [5–7,37–39].

Novel microcrystalline scheelite-type $Cd_{1-3x}\square_xRE_{2x}MoO_4$ solid

* Corresponding author.
E-mail address: tomela@zut.edu.pl (E. Tomaszewicz).
Peer review under responsibility of The Chinese Ceramic Society.

https://doi.org/10.1016/j.jmat.2020.12.010

Please cite this article as: B. Sawicki, E. Tomaszewicz, T. Groń *et al.*, Dipole relaxation process and giant dielectric permittivity in Eu^{3+}-doped $CdMoO_4$ single crystal, Journal of Materiomics, https://doi.org/10.1016/j.jmat.2020.12.010

solutions (RE = Pr, Nd, Sm − Yb) have been synthesized earlier by us using high-temperature annealing of adequate mixtures of $CdMoO_4$ with $RE_2(MoO_4)_3$ [11,29–31,40,41]. The substitution of Cd^{2+} ions by trivalent RE^{3+} ones in $CdMoO_4$ matrix gives rise to excessive positive charge which is compensated by the appearance of vacancies (□) in the scheelite framework [11,29–31,40,41]. Single crystals of some $Cd_{1-3x}□_xRE_{2x}MoO_4$ solid solutions (RE = Nd, Gd, and Dy) were grown by the Czochralski technique [42–44]. The Dy^{3+} as well as Nd^{3+}-doped cadmium molybdate single crystals are known to show unique dielectric and magnetic properties [42,44]. In particular, $Cd_{1-3x}□_xNd_{2x}MoO_4$ ($x = 0.014$) single crystal reveals a paramagnetic state with short-range ferromagnetic interactions and a strong anisotropy of other properties, *i.e.* metallic conductivity with a *p-n* transition and dielectric constant ε_r ~60 ÷ 100 along [100] crystallographic direction as well as semiconductor behaviour with *n-p* transition and ε_r ~ 750 ÷ 2250 along [001] plane [42]. Diode-like behaviour visible on the *I–V* characteristics was also observed for this crystal [42]. These crystal properties were explained in terms of relaxation processes [45,46] or as anisotropic relaxor ferroelectric like behaviour [47].

In the present work, we applied the Czochralski technique to grow scheelite-type Eu^{3+}-doped cadmium molybdate single crystal. The growth process was carried out in air under 1 MPa. The purpose of this article is to investigate the structural, optical, magnetic and electrical properties of the as-grown crystal along the [100] and [001] crystallographic directions. Dielectric analysis in the frequency representation including the Cole-Cole fit to examine the dipole relaxation process within the temperature range of 76–400 K, was made.

2. Experimental

2.1. Crystal growth and chemical analysis of Eu^{3+}-doped cadmium molybdate single crystal

Single crystal of $Cd_{1-3x}□_xEu_{2x}MoO_4$ solid solution ($x = 0.0048$ and □ denotes vacancies, labelled later as $CdMoO_4:Eu^{3+}$) was successfully grown by the Czochralski method in an inductively heated platinum crucible in air atmosphere under 1 MPa. Starting materials for the crystallization process were the following oxides: Eu_2O_3 (5.6923 g (0.0162 mol); 99.99%, Alfa Aesar), CdO (78.8917 g (0.6144 mol); 99.998%, Alfa Aesar), and MoO_3 (95.4140 g (0.6629 mol); 99.95%, Alfa Aesar). The total mass of all metal oxides used for the pulling of single crystal was 180.0000 g. The stoichiometric amounts of starting reactants were ground homogeneously in an agate mortar, pressed into cylindrical pellets under pressure of 200 kPa and heated at 1073 K for 12 h in air before their melting in a platinum crucible. Afterwards, the microcrystalline material was heated up to a temperature ~50 K, higher than its melting point, under 1 MPa. The obtained melt was maintained in these conditions for 2 h. Next, its temperature was decreased to the appropriate crystallization point. The single crystal of cadmium molybdate doped with Eu^{3+} was grown on the [001] oriented seed prepared from a single crystal of pure cadmium molybdate at the 3 mmh^{-1} pulling rate and 10 rpm rotating rate. After crystallization, the obtained single crystal was pulled out of the melt and cooled down to room temperature at the rate of 10–30 K h^{-1}. The $CdMoO_4:Eu^{3+}$ single crystal, grown in air atmosphere, is dark-blue in colour. After accurate orientation by X-ray diffraction, the $CdMoO_4:Eu^{3+}$ single crystal was cut along the [100] and [001] crystallographic planes, and then plates of dimensions of ~5 × 6 × 1 mm were cut off (Fig. 1). As-prepared samples of $CdMoO_4:Eu^{3+}$ crystal were used for the optical, magnetic and dielectric studies. For X-ray diffraction measurements, small pieces of diameters less than 0.1 mm were cut off the as-grown single crystal and selected under a polarization microscope. The contents of europium, cadmium and molybdenum in $CdMoO_4:Eu^{3+}$ single crystal were determined by an Inductively Coupled Plasma Mass Spectrometry (ICP-MS) technique. The contents of these elements were found as: Eu 2.71(2) mas% (cal. 2.73 mas%), Cd 38.33(3) mas% (cal. 38.37 mas%), and Mo 35.28(5) mas% (cal. 35.33 mas%). The determined contents of Eu, Cd, and Mo in $CdMoO_4:Eu^{3+}$ single crystal closely corresponded to the proposed chemical formula. Density of as-grown $CdMoO_4:Eu^{3+}$ single crystal was determined using a Quantachrome Instruments Ultrapycnometer (model Ultrapyc 1200 e, USA). As a pycnometric gas nitrogen (purity 99.99%) was applied. This value was found to be 6.09(1) g cm^{-3}. Small pieces of $CdMoO_4:Eu^{3+}$ single crystal obtained during cutting out the samples for optical, magnetic as well as electrical studies, were ground in an agate mortar. The obtained powder as well as microcrystalline $CdMoO_4$ synthesized by high-temperature sintering of CdO/MoO_3 mixture were examined by powder X-ray powder diffraction method using an EMPYREAN II diffractometer (PANalytical) and $CuK\alpha_{1,2}$ radiation ($\lambda = 0.15418$ nm). XRD patterns were collected within the 10–100° 2Θ range with the scanning step of 0.013° and analysed by a HighScore Plus 4.0 software. Lattice constants were calculated using a DICVOL04 software [48]. Fig. 2 shows the XRD patterns of powdered $CdMoO_4:Eu^{3+}$ single crystal and pure $CdMoO_4$. According to XRD analysis, the powder diffraction patterns of both materials consisted of only diffraction peaks which can be attributed to a scheelite-type framework. No additional phases were observed. All peaks were successfully indexed to pure tetragonal, body-centered scheelite-type structure with space group $I4_1/a$ (JCPDs No. 01-088-0182).

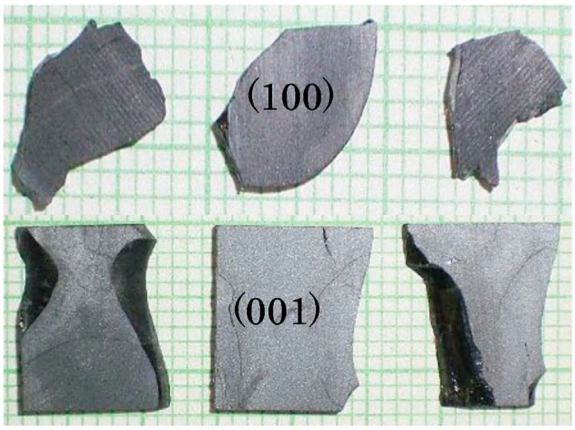

Fig. 1. Images of $CdMoO_4:Eu^{3+}$ single crystal in (100) and (001) planes.

2.2. Methods

X-ray diffraction measurements of $CdMoO_4:Eu^{3+}$ single crystal were performed with an Oxford Diffraction kappa diffractometer Xcalibur with MoKα radiation and a Sapphire3 CCD detector (Oxford Diffraction Ltd., Yarnton, UK) at 298(1) K. For the measurements a small sample of the single crystal was mounted on a glass capillary. The data were collected using a CrysAlis CCD program

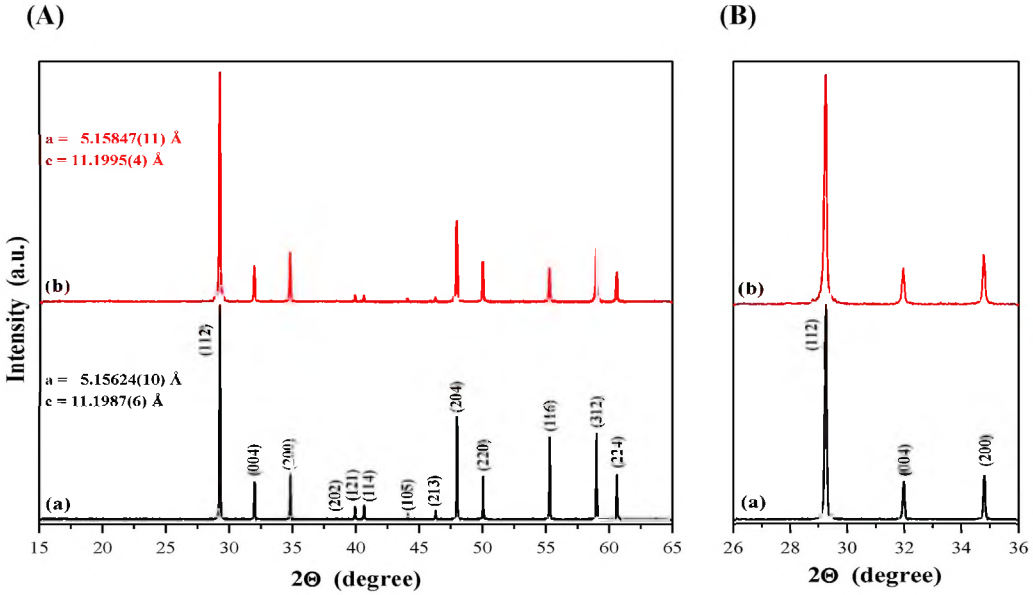

Fig. 2. Powder XRD patterns of $CdMoO_4$ (a) and powdered $CdMoO_4$:Eu^{3+} single crystal (b) in the range of 2Θ from 15 to 65° (A) and the (112/004/200) diffraction lines in the range of 2Θ from 26 to 36° (B).

[49]. Accurate cell parameters were determined and refined also with CrysAlis CCD program [49] from ca. 1700 reflections. For the integration of collected data the program CrysAlis RED was used. The scheelite-type structure of $CdMoO_4$:Eu^{3+} single crystal was refined using the SHELXL-97 program [50]. The positions of O atoms and anisotropic displacement parameters of all atoms were refined. Ultraviolet–visible (UV–vis) diffuse reflectance spectroscopy was realized with a JASCO-V670 (Japan) spectrophotometer equipped with an integrating sphere. The spectra were recorded in the range from 200 to 1000 nm. Static magnetic susceptibility, $\chi(T)$, was measured within the temperature range of 2–300 K and in the magnetic field $H = 1$ kOe and recorded both in zero-field-cooled (ZFC) and field-cooled (FC) mode. Magnetization isotherms, $M(H)$, were measured at 2, 10, 20, 40, 60, and 300 K and in the static magnetic field up to 70 kOe. For these studies, a Quantum Design MPMS-XL-7AC SQUID magnetometer (USA) was used. Electrical conductivity, $\sigma(T)$, of $CdMoO_4$:Eu^{3+} single crystal was measured by the DC method using a KEITHLEY 6517B Electrometer/High Resistance Meter (USA). The activation energy, E_a, for the clearly straight intervals was calculated in the temperature range of 100–250 K from the formula $\sigma = \sigma_0 \exp(-E_a/kT)$, where k is the Boltzmann constant. The values of the thermal coefficient of resistance (TCR), α_{TCR}, were estimated from the relation $\rho = \rho_0(1 + \alpha_{TCR} \cdot \Delta T)$. Thermoelectric power, $S(T)$, was measured within the temperature range of 100–400 K using a Seebeck Effect Measurement System (MMR Technologies, Inc., USA). Broadband dielectric spectroscopy measurements were performed using a LCR HITESTER (HIOKI 3532–50, Japan) within the temperature range of 76–400 K and in the frequency range from $2 \cdot 10^2$ to $2 \cdot 10^6$ Hz. The electrode area and thickness were 5 mm^2 and 1.0 mm, respectively. For measurements of $\varepsilon_r = C/C_0$, where C_0 is the capacity of the empty capacitor and $\tan\delta = \varepsilon''/\varepsilon'$, where ε'' and ε' are imaginary and real part of complex dielectric permittivity, respectively, the electric field was applied along the [100] and [001] directions. The electrical and thermal contacts were made with a silver lacquer mixture (Degussa Leitsilber 200).

3. Results and discussion

3.1. X-ray diffraction studies and structure of $CdMoO_4$:Eu^{3+} single crystal

X-ray diffraction measurement at 298(1) K of $CdMoO_4$:Eu^{3+} single crystal showed that this material crystallizes in tetragonal scheelite-type structure with space group $I4_1/a$ (Fig. 3) analogously to other divalent and scheelite-type molybdates and tungstates, *i.e.* $PbMoO_4$ and $PbWO_4$ [51]. The lattice parameters of unit cell are: $a = b = 5.16188(14)$ and $c = 11.2080(5)$ Å and the agreement factor $R1 = 2.61\%$ (Table 1). The atomic coordinates and equivalent isotropic thermal parameters of Eu^{3+}-doped single crystal are shown in Table S1. Molybdenum ions occupy tetrahedral positions and form deformed MoO_4 tetrahedra, while Cd^{2+}/Eu^{3+} ones are dodecahedrally coordinated by oxygen ions (Tables S1 and S2). The Eu^{3+} ions do not show long-range order and they are randomly distributed in cadmium molybdate framework, substituting Cd^{2+} ones. Similar distribution of other RE^{3+} ions, *i.e.* Nd^{3+}, Gd^{3+}, Dy^{3+} (in $Cd_{1-3x}\square_x RE_{2x}MoO_4$) [42–44] and Yb^{3+} (in $Cd_{1-3x}\square_x RE_{2x}(MoO_4)_{1-3x}(WO_4)_{3x}$ [52]) has been observed in other doped scheelite-type single crystals obtained by us earlier.

To assign the oxidation state of cadmium, europium and molybdenum centres, we applied the calculation based on the bond valence sum (BVS) model [53,54]. In this procedure, the valence S of a bond between two atoms i and j is expressed by the empirical expression (Eq. (1)), where R_{ij} is the length of the bond (in Å), the constants b and R_0 are known [55,56]. The constant b is 0.37, which has been determined by Brown and Altermatt and is generally accepted for most ij pairs. The value R_0 can be considered as a bond length of unit valence and it is dependent upon the nature of the ij pair of atoms [57].

$$S_{ij} = \exp\left(\frac{R_0 - R_{ij}}{b}\right) \quad (1)$$

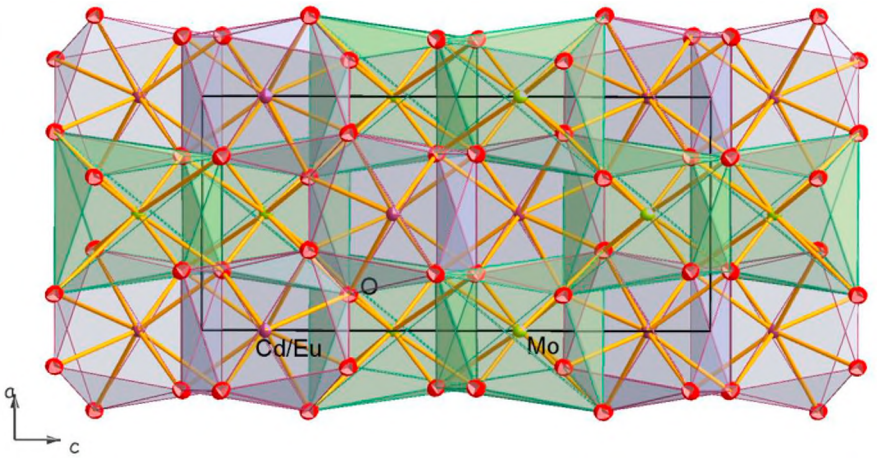

Fig. 3. Scheelite-type structure of $CdMoO_4:Eu^{3+}$ single crystal. The Cd^{2+}/Eu^{3+}, Mo^{6+} and O^{2-} ions are marked in wine, red and green, respectively. Ellipsoids representing displacement parameters are drown at the 50% probability level. The *a* and *c* are crystallographic axes corresponding of the notation [100] and [001], respectively.

Table 1
Crystal data collection and structure refinement for $CdMoO_4:Eu^{3+}$.

Crystal data	
Empirical formula	$Cd_{0.9268}Eu_{0.0488}MoO_4$
M_r (g/mol)	272.34
Crystal system, space group	tetragonal, $I4_1/a$
Temperature (K)	293(1) K
Crystal size (mm)	0.02 × 0.08 × 0.15
a, b, c (Å)	5.16188(14), 5.16188(14), 11.2080(5)
α, β, γ (°)	90, 90, 90
V (Å^3)	298.638(17)
Z, calculated density	4, 6.057 Mg/m^3
Radiation type, wavelength	Mo *Kα*, 0.71073 Å
μ (mm^{-1})	11.131
F(000)	488
Data collection	
Diffractometer	Xcalibur (Oxford Diffraction) with MoK radiation and Sapphir3 CCD detector
Theta range (°)	4.35–34.47
Limiting indices	$-7 \le h <= 5$, $-7 \le k <= 8$, $-17 \le l <= 17$
Reflections collected/unique	1755, 312
R_{int}	0.0288
Completeness to θ = 25.42°	100.0%
Refinement	
Data/restraints/parameters	312/0/16
R[$F^2 > 2\sigma(F^2)$], wR(F^2), S	R1 = 0.0210, wR2 = 0.0471, 1.09
R indices (all data)	R1 = 0.0344, wR2 = 0.0525
Extinction coefficient	0.0104(8)
Δ_{max}, Δ_{min} (e Å^{-3})	0.886, −0.654

Table 2
Bond valence values for cadmium, europium and molybdenum.

Element, polyhedron	Length of the bond (Å)	R_0 (Å)	BVS
Cadmium	2.4012(16) × 4	1.875(13)	1.891
$Cd^{II}O_8$	2.4163(17) × 4		
Europium	2.4012(16) × 4	2.038	2.938
$Eu^{III}O_8$	2.4163(17) × 4		
Molybdenum	1.7777(17) × 4	1.900	5.567
$Mo^{VI}O_4$			

The oxidation number N_i of the atom *i* is an algebraic sum (Eq. (2)) of these S_{ij} values of all the bonds (*n*) around the atom, *i*.

$$N_i = \sum_{i=1}^{n} S_i \quad (2)$$

The calculated BSV values are as follows: Cd(II) 1.891; Eu(III) 2.938; Mo(VI) 5.567 and are shown in Table 2. The BVS value for Mo could indicate the presence of a small amount of Mo^{5+} ions.

3.2. UV–vis diffuse reflectance spectra and optical band gap

Optical properties of $CdMoO_4:Eu^{3+}$ single crystal along both crystallographic directions were investigated at room temperature by using UV–vis diffuse reflectance spectroscopy. This technique takes advantage of the enhanced scattering in solid materials. The theory which makes possible to use diffuse reflectance spectra was proposed by Kubelka and Munk [58]. According to this method, the reflectance spectra were converted into absorption ones using the following equation [58]:

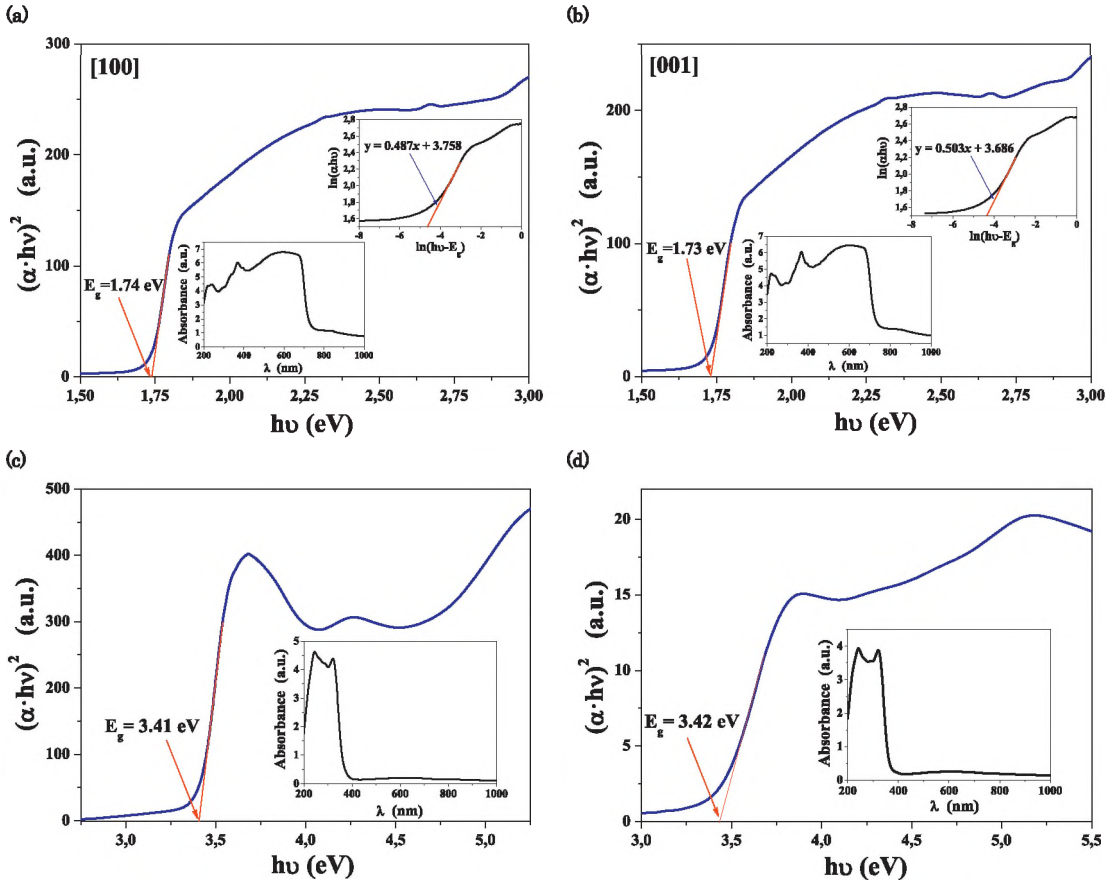

Fig. 4. Plots of $(\alpha h\nu)^2$ *vs.* hν of $CdMoO_4:Eu^{3+}$ single crystal along [100] (a) and [001] (b) crystallographic directions, powder sample of $CdMoO_4$ (c), and powder piece of $CdMoO_4:Eu^{3+}$ single crystal (d). Inset: UV–vis absorption spectra for all samples as well as plots of $\ln(\alpha h\nu)$ *vs.* $\ln(h\nu\text{-}E_g)$ for $CdMoO_4:Eu^{3+}$ single crystal for both crystallographic directions.

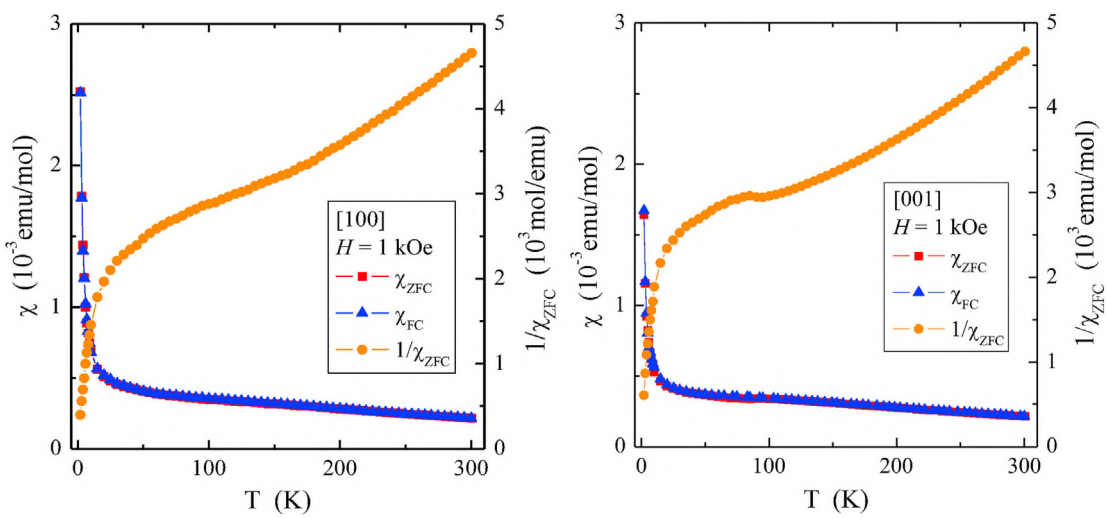

Fig. 5. ZFC and FC magnetic susceptibility χ and $1/\chi_{ZFC}$ *vs.* temperature *T* at $H = 1$ kOe measured along [100] and [001] directions.

$$F(R) = \frac{\alpha}{S} = \frac{(1-R)^2}{2R} \tag{3}$$

where $F(R)$ is the Kubelka–Munk approach, R is the reflectance, α is the absorption coefficient, and S is the scattering factor which is wavelength independent. Optical band energy (E_g) is related to the absorbance and photon energy the equation proposed by Tauc and Wood [59,60]:

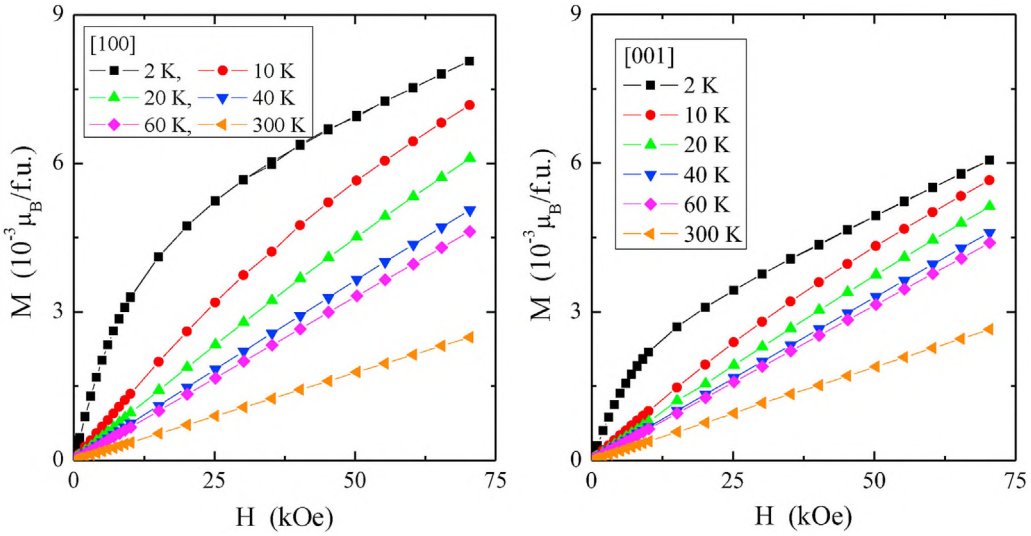

Fig. 6. Magnetization M *vs.* magnetic field H at 2, 10, 20, 40, 60 and 300 K measured along [100] and [001] directions.

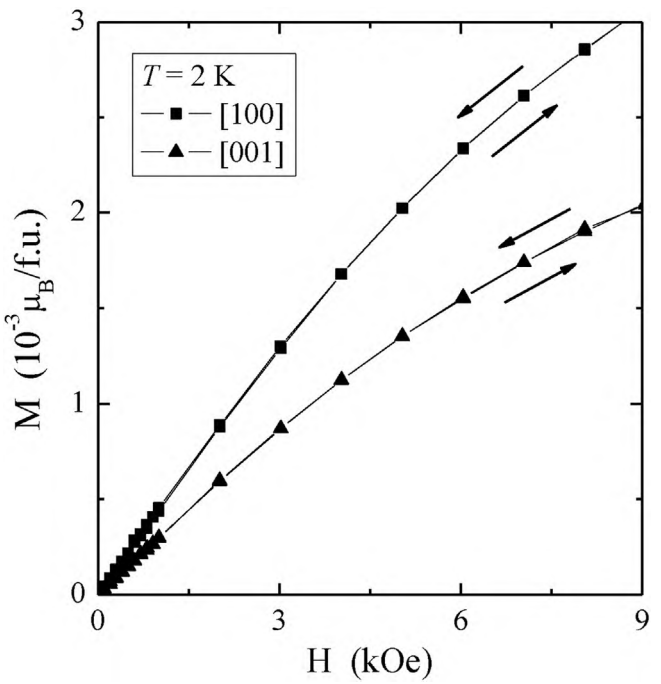

Fig. 7. Magnetization M *vs.* magnetic field H at 2 K for both directions. The arrows indicate the primary magnetization curve and the return one, their overlapping means no hysteresis loop.

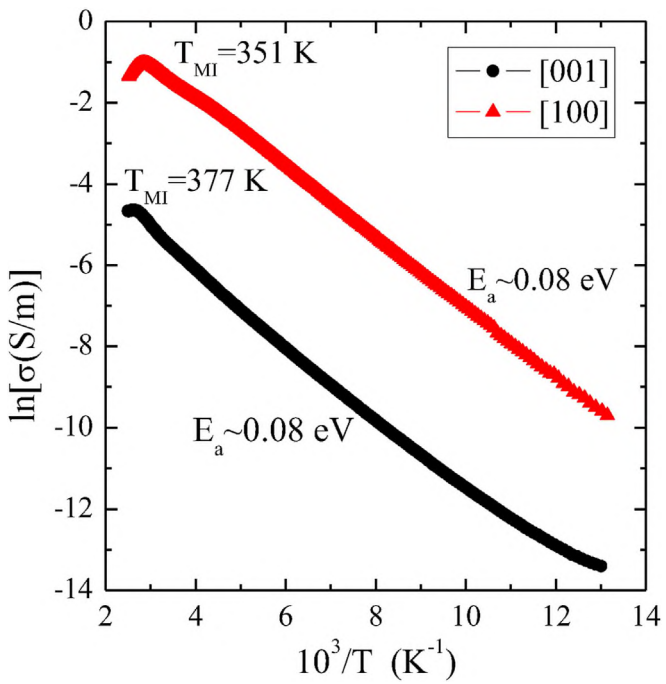

Fig. 8. Electrical conductivity σ *vs.* reciprocal temperature $10^3/T$ measured along [100] and [001] directions. T_{MI} is the temperature of the metal-insulator transition, and E_a is the activation energy.

$$\alpha h\nu = F(R)\cdot h\nu = (h\nu - E_g)^n \quad (4)$$

where $h\nu$ is the photon energy, A is an energy independent constant characteristic of a material, and n is a constant that can take different values depending on the nature of electronic transition. The permitted direct, forbidden direct, permitted indirect and forbidden indirect transitions take place for $n = 1/2$, 3/2, 2, and 3, respectively [59,60]. Therefore, the optical band gap energy can be determined from the plot of $(\alpha h\nu)^{1/n}$ versus photon energy by extrapolating a linear portion of this dependence to intersect the $h\nu$ axis at zero absorption [61–70]. The plots of $(\alpha h\nu)^2$ *vs.* $h\nu$ for $CdMoO_4:Eu^{3+}$ single crystal are depicted in Fig. 4a and b. The band gap energy of this crystal is found to be 1.74 eV along the [100] and 1.73 eV along the [001] directions, corresponding to a direct permitted transition of an electron between valence and conduction bands. In the high energy region of the absorption edge, $(\alpha h\nu)^2$ varied linearly with photon energy. Thus, in the low energy region, the absorption spectrum deviated from a straight line plot. This straight line behaviour in the high energy region was taken as prime evidence of a direct optical band gap. Furthermore, the curves of $\ln(\alpha h\nu)$ *vs.* $\ln(h\nu - E_g)$ were plotted using E_g to confirm the value of n from the slope of these curves. The values of 0.487 and

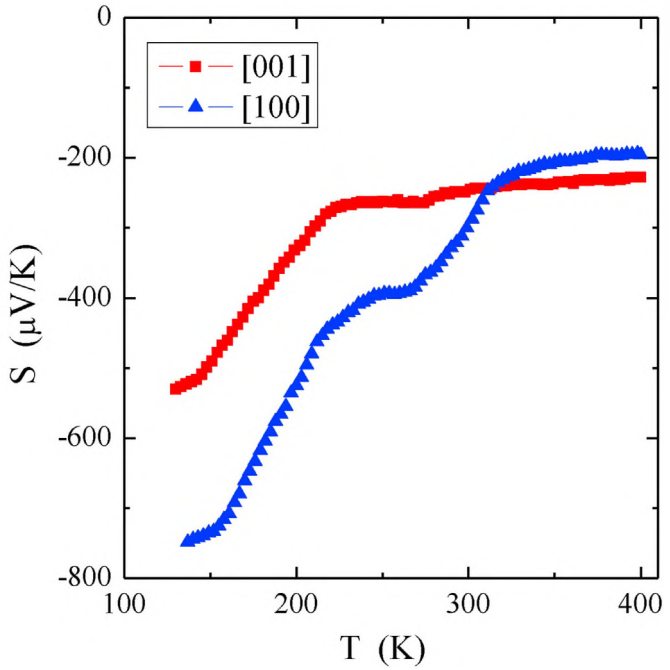

Fig. 9. Thermoelectric power *S* *vs.* temperature *T* measured along [100] and [001] directions.

0.503 have been found for [100] and [001] crystallographic directions, respectively (Fig. 4a and b). The determined values of n parameter (very close to 0.5) confirm that the as-grown $CdMoO_4$:Eu^{3+} single-crystal is a direct gap semiconductor. The E_g values are very close to the ones estimated for the other scheelite-type single crystals obtained by us, *i.e.* Nd^{3+}-doped $CdMoO_4$ [42] and Yb^{3+}-doped $Cd(Mo,W)O_4$ [52]. We also found that E_g values obtained for $CdMoO_4$:Eu^{3+} single crystal are twice smaller than that determined for microcrystalline cadmium molybdate (3.41 eV, Fig. 4c), obtained by high-temperature sintering of stoichiometric CdO/MoO_3 mixture, as well as for powder $CdMoO_4$:Eu^{3+} single crystal (3.42 eV, Fig. 4d).

3.3. Magnetic properties

The temperature dependence of magnetic susceptibility, χ(T), measured along the [100] and [001] directions within the temperature range of 2–300 K (Fig. 5) corresponded to paramagnetic behaviour with the overlapping magnetic susceptibilities of ZFC and FC mode. This means no spin frustration, and the lack of the Curie-Weiss region, *i.e.* no linearity of the inverse of magnetic susceptibility in the high-temperature regime. The shape of magnetic isotherms, *M*(H), recorded at 2, 10, 20, 40, 60 and 300 K (Fig. 6) showed neither saturation magnetization at 2 K nor magnetic hysteresis for both directions, because in the latter case the primary magnetization curve coincided with the return one (Fig. 7) resulted in no remanence and coercive field. The *M*(H) dependence becomes linear with increasing temperature, indicating paramagnetic response. Both magnetic susceptibility and magnetization have slightly higher values along the [100] direction than along the [001] one. The weak paramagnetism of the $CdMoO_4$:Eu^{3+} single crystal results from the fact that the europium ions (like samarium ones) have narrow multiplets comparable to the thermal energy of *kT* [71]. So, that not all the atoms are in their ground state [72], and therefore the levels above this ground state may not contribute to the magnetic susceptibility [73]. Similar behaviour was observed for Sm_2WO_6 and Eu_2WO_6 [74], $Co_2Sm_2W_3O_{14}$ [75], $Co(Sm,Eu)_4W_3O_{16}$ and $Zn(Sm,Eu)_4W_3O_{16}$ [76].

3.4. Electrical properties

Electrical conductivity (Fig. 8) and thermoelectric power (Fig. 9) measurements indicated *n*-type semiconducting properties of $CdMoO_4$:Eu^{3+} single crystal with the activation energy of $E_a = 0.08$ eV, regardless of the crystallographic direction, as well as the metal-insulator transition at $T_{MI} = 351$ K along the [100]

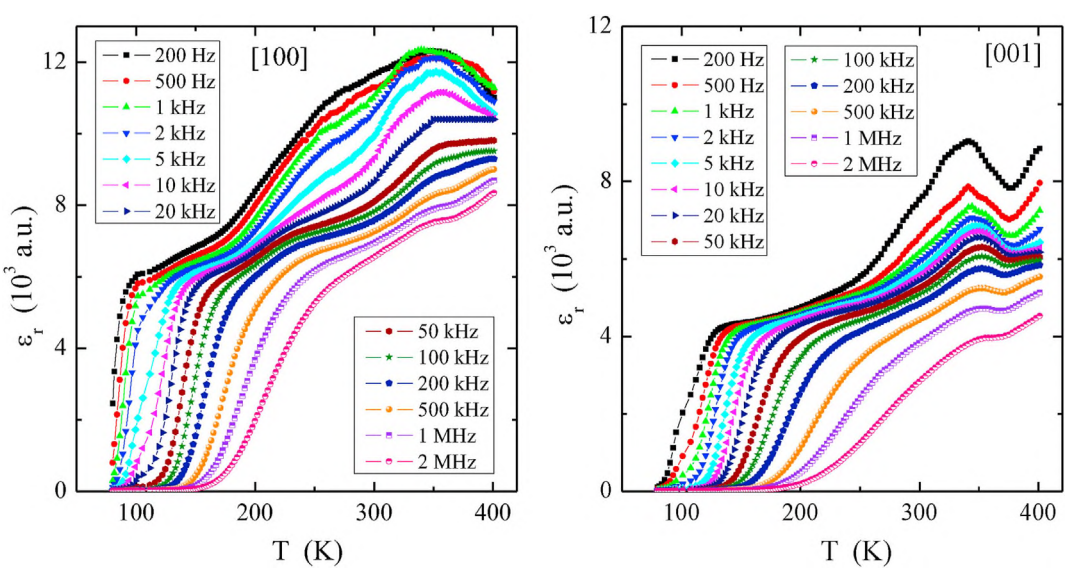

Fig. 10. Relative permittivity ε_r *vs.* temperature *T* at ν = 200 Hz, 500 Hz, 1 kHz, 2 kHz, 5 kHz, 10 kHz, 20 kHz, 50 kHz, 100 kHz, 200 kHz, 500 kHz and 1 MHz measured along [100] and [001] directions.

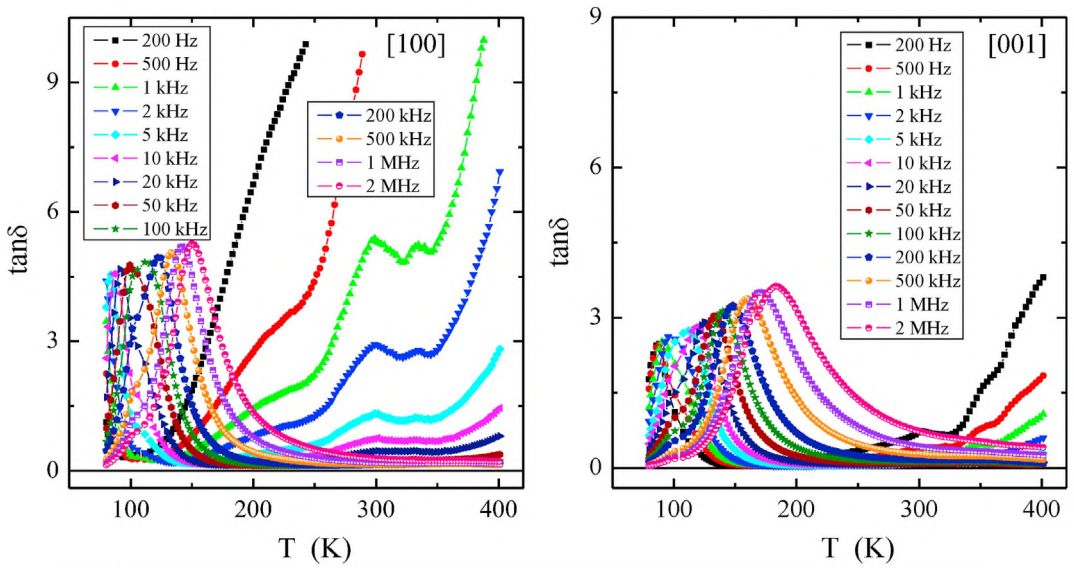

Fig. 11. Loss tangent tanδ *vs.* temperature *T* at ν = 200 Hz, 500 Hz, 1 kHz, 2 kHz, 5 kHz, 10 kHz, 20 kHz, 50 kHz, 100 kHz, 200 kHz, 500 kHz and 1 MHz measured along [100] and [001] directions.

direction with lower conductivity and at T_{MI} = 377 K along the [001] one, with higher conductivity. The metal-insulator transition, T_{MI}, is visible here by changing the sign of the thermal resistance coefficient, α_{TCR}, from −1.14 to +0.17 K^{-1} and from −2.48 to +0.18 K^{-1} for directions [001] and [100], respectively. Unexpectedly, for the single crystal under study, the relative permittivity, ε_r (Fig. 10), above room temperature reached values of 8,000 and 12,000 along the [001] and [100] directions, respectively. Such great relative permittivity is characteristic of microcrystalline materials and in this case it can be associated with a strong charge accumulation when the width of Eu^{3+}-multiplet becomes comparable to the thermal energy *kT*. The loss tangent, tanδ, depicted in Fig. 11 is large and strongly depends on temperature and frequency for both directions.

3.5. *Dielectric studies*

A step-like behaviour of dielectric permittivity, ε_r, observed for both crystallographic directions in Fig. 10, shifting to lower temperatures with decreasing frequency, indicates the existence of the dipole relaxation process is most likely derived from the jump of ions along the empty spaces in the crystal. This relaxation is also manifested as a peak in the temperature dependence of tanδ (Fig. 11). For further analysis of this relaxation process, the dielectric data were presented in Fig. 12 as frequency dependent dielectric permittivity, ε', and dielectric loss, ε'', spectra, respectively. In this representation the dipole process is visible as a step in the $\varepsilon'(\nu)$ and relaxation peak in the $\varepsilon''(\nu)$ spectra, respectively. This relaxation process shifts to lower frequencies on cooling, *i.e.* it becomes slower with decreasing temperature. To check qualitatively if there are differences between the dielectric results collected for different crystallographic directions, the $\varepsilon'(T)$ and $\varepsilon''(T)$ data for two selected frequencies, 5 kHz and 500 kHz, respectively, were compared in Fig. 13. It is clearly visible that relaxation at the spectra for the [100] direction are shifted to lower temperatures relative to those for the [001] one. This shift suggests that dipole relaxation process observed in the doped single crystal should have different time scale for the same temperatures, depending of the crystallographic direction. This difference becomes obvious when the $\varepsilon''(\nu)$ spectra measured for the same temperature but different crystallographic directions are compared (Fig. 14). The relaxation process visible as the bell-like peak for the [001] direction is around one order of magnitude slower than for the [100] one. Additionally, at lower frequencies, the ion conductivity process is visible as the linear bending up of $\varepsilon''(\nu)$-dependence. This observation indicate on formation of different number of vacancies for different directions that results in various time of relaxation of the dipole moment.

To estimate the temperature behaviour of the dipole relaxation process, the imaginary part of the complex dielectric permittivity, $\varepsilon^*(\nu)$, *i.e.* the dielectric loss data, $\varepsilon''(\nu)$, collected for both crystallographic directions were fitted by sum of the conductivity part and the Cole-Cole equation (describing relaxation process, see inset in Fig. 14) [77]:

$$\varepsilon''(\omega) = \mathbf{Im}\left(\varepsilon_\infty + \frac{\Delta\varepsilon}{1+(i\omega\tau)^\alpha}\right) + \frac{\sigma_{DC}}{\varepsilon_0\omega} \quad (5)$$

where σ_{DC} is the dc conductivity, α is the shape parameter describing symmetric broadening of the relaxation curve, Δε is the dielectric strength and τ is the relaxation time. Analytical form of this equation, used during the fitting procedure is presented as follows:

$$\varepsilon''(\omega) = \Delta\varepsilon\left(1+2(\omega\tau)^\alpha\cos\left(\pi\alpha/2\right)+(\omega\tau)^{2\alpha}\right)^{-1/2}\sin\varphi \quad (6)$$

where

$$\varphi = arctan\left(\frac{(\omega\tau)^\alpha\sin\left(\pi\alpha/2\right)}{1+(\omega\tau)^\alpha\cos\left(\pi\alpha/2\right)}\right) \quad (7)$$

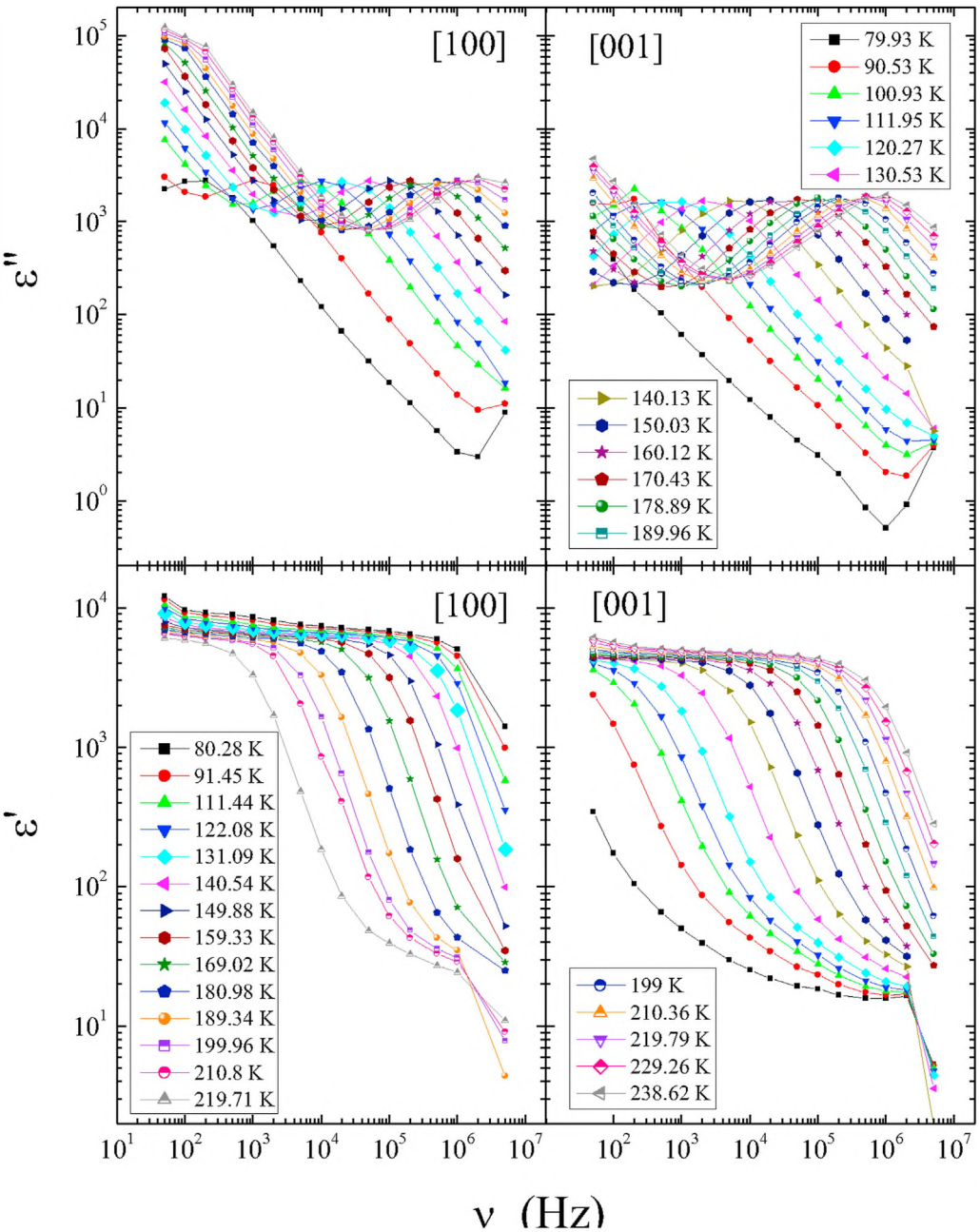

Fig. 12. Real (ε') and imaginary (ε'') components of permittivity *vs.* frequency ν measured along [100] and [001] within the temperature range of 79–239 K in which the presence of the relaxation process is visible. These data have been transformed into the frequency domain from the data presented in Figs. 8 and 9.

It should be mentioned that for the further analysis only the dielectric loss data were used. Because the $\varepsilon'(\nu)$ and $\varepsilon''(\nu)$ are interrelated by the Kramers–Kronig relations [78], it was not necessary to analyse both components of the complex dielectric permittivity, $\varepsilon^*(\nu)$.

Relaxation times estimated using Eq. (5) are presented as a function of temperature in Fig. 15. In this plot, τ exhibits a nonlinear dependence on temperature that was well parameterized with use of Arrhenius equation $\tau = \tau_0 \exp\left(\frac{E_a}{kT}\right)$, where E_a is the activation energy and k is the Boltzmann constant. The estimated value of $E_a = 0.127 \pm 0.001$ eV was the same for both crystallographic directions and constant in the range from the high temperature limit down to ca. 120 K, as follows from the linear dependences of τ *vs.* $10^3/T$ depicted in the inset to Fig. 15. It should be emphasized that, although for both directions the estimated values of E_a are the same, the τ(T) dependence in the [100] crystallographic direction is shifted to shorter times (in the same temperatures) in comparison to that obtained for the [001] direction. The same behaviour was observed in perovskite-like methylhydrazinium zinc formate [79].

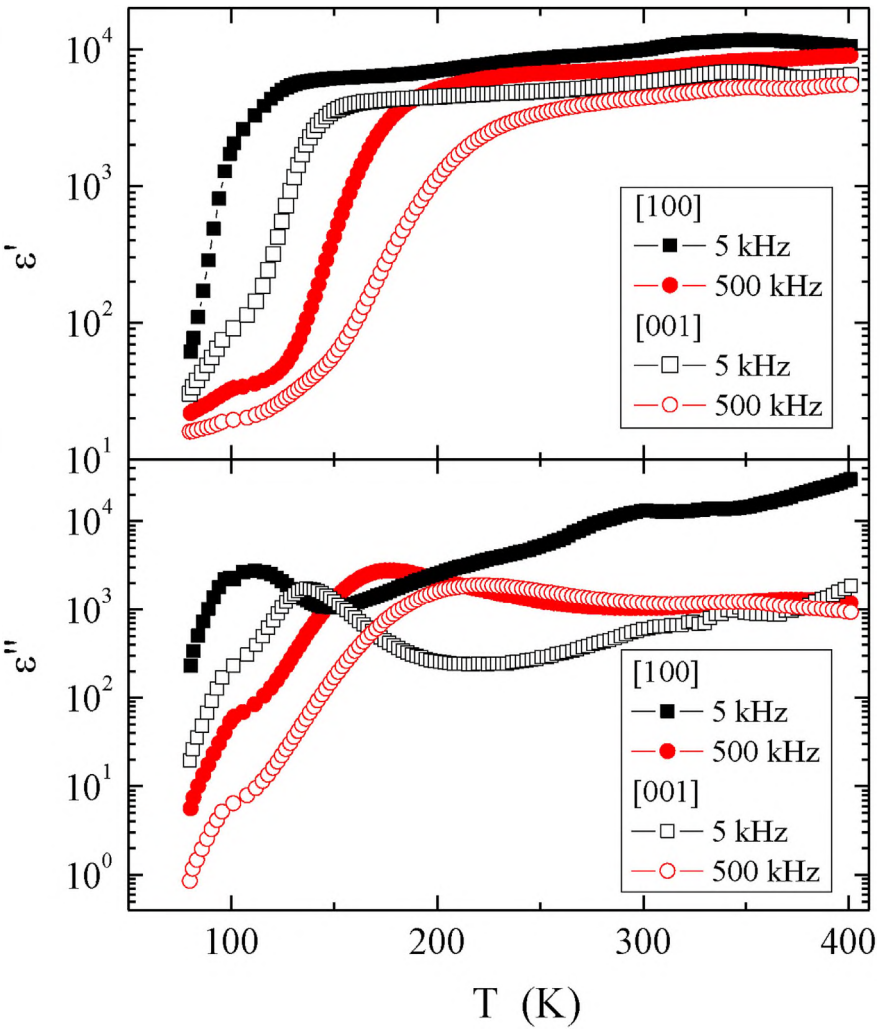

Fig. 13. Real (ε') and imaginary (ε'') components of permittivity *vs.* temperature *T* measured along [100] and [001] directions for two selected frequencies, *i.e.* 5 and 500 kHz. One can see clear differences depending on the crystallographic direction.

Moreover, it is worth noting that for temperatures lower than ca. 120 K the departure from linear behaviour of $\tau(10^3/T)$ is observed for both crystallographic directions. On further cooling below 100 K, the $\tau(T)$ behaviour seems to be still activation-like (linear $\tau(10^3/T)$ dependence at the Arrhenius plot in the inset to Fig. 15). However, due to limited temperature range, a reliable parameterization of this dependence was difficult.

4. Conclusions

In summary, a single crystal of Eu^{3+}-doped cadmium molybdate ($Cd_{1-3x}\square_xEu_{2x}MoO_4$, where $x = 0.0048$ and denotes vacancies) was successfully grown by the Czochralski technique in air atmosphere and under 1 MPa. The as-grown single crystal belongs to tetragonal scheelite-type structure (space group $I4_1/a$). The magnetic and electrical results revealed paramagnetism in both crystallographic directions, the *n*-type semiconducting behaviour with the metal-insulator transition above 350 K as well as an unexpected colossal dielectric permittivity above room temperature, which reached values of 8,000 and 12,000 along the [001] and [100] directions, respectively. Analysis of the loss component of complex dielectric permittivity using the Cole-Cole fit and taking into account the contribution from the electrical conductivity, showed that the dipole relaxation process of the Arrhenius type, manifested as a peak in the temperature dependence of the tanδ, is visible at lower temperatures with decreasing frequency and this process becomes slower with decreasing temperature. Moreover, time scale of this relaxation differs with crystallographic direction and is ca. order of magnitude slower along the [001] direction. On the other hand, along both directions activation energy of the relaxation is the same. Above room temperature, the relaxation is accompanied by colossal dielectric permittivity. These unexpected results are due to the fact that the width of the europium multiplets becomes comparable to the thermal energy *kT* on heating.

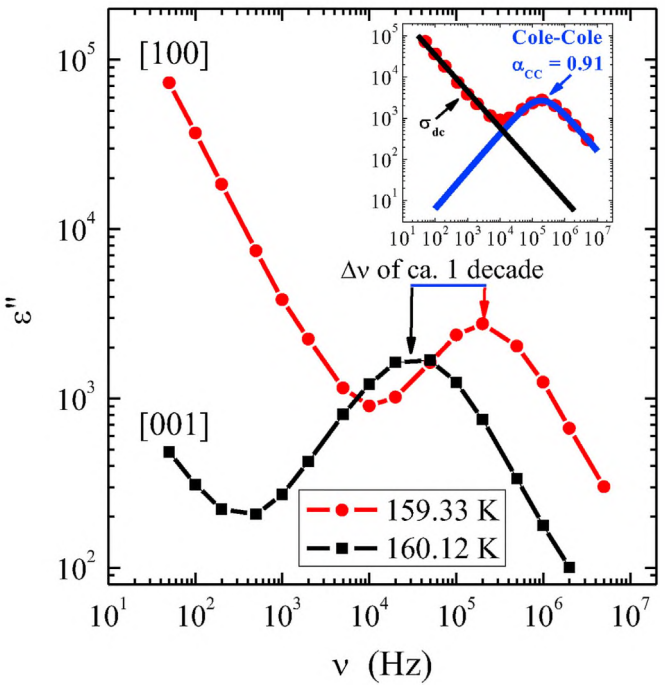

Fig. 14. Comparison of dielectric loss spectra, $\varepsilon''(\nu)$, measured for [001] (black squares) and [100] (red circles) crystallographic directions for almost the same temperature. Inset: spectrum measured for direction [100] with Cole-Cole and conductivity fitting functions.

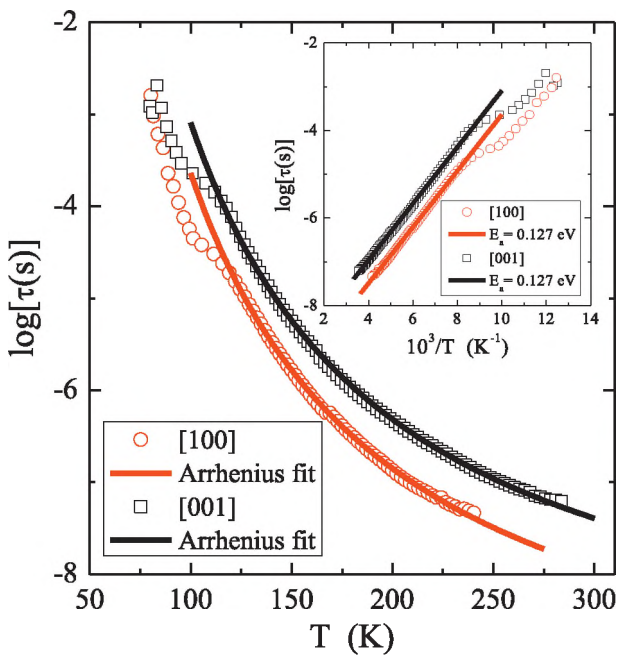

Fig. 15. Temperature dependence of dielectric relaxation time (logτ) estimated for [001] (black squares) and [100] (red circles) crystallographic directions. The fitting curves were calculated from the Arrhenius equation. Inset: logτ vs. $10^3/T$ (the Arrhenius plot) of data from the main part of this Figure. The straight solid lines represent the Arrhenius range of the relaxation time with the activation energy of $E_a = 0.127$ eV for both directions. $\tau_0 = 0.087$ ns and 0.29 ns for [100] and [001] directions, respectiely.

Declaration of competing interest

The authors declare that they have no known competing financial interests or personal relationships that could have appeared to influence the work reported in this paper.

Acknowledgements

The authors thank Mr. Waldemar Szymański from Department of Physics (West Pomeranian University of Technology in Szczecin, Poland) for his help in crystal growth. The authors are also grateful to the team workshop of the Institute of Physics (University of Silesia) for providing practical and technical assistance.

Appendix A. Supplementary data

Supplementary data to this article can be found online at https://doi.org/10.1016/j.jmat.2020.12.010.

References

[1] Lei F, Yan B. Hydrothermal synthesis and luminescence of $CaMoO_4$:RE^{3+} (M = W, Mo; RE = Eu, Tb) submicro-phosphors. J Solid State Chem 2008;181:855–62.
[2] Campos AB, Simões AZ, Longo E, Varela JA, et al. Mechanisms behind blue, green, and red photoluminescence emissions in $CaWO_4$ and $CaMoO_4$ powders. Appl Phys Lett 2007;91. 051923.
[3] Bouzidi C, Ferhi M, Elhouichet H, Ferid M. Structural and luminescence properties of $(Ba_{1-x}Eu_x)MoO_4$ powders. J Lumin 2016;179:230–5.
[4] Guzik M, Tomaszewicz E, Kaczmarek SM, Cybińska J, et al. Spectroscopic investigations of $Cd_{0.25}Gd_{0.50}\square_{0.25}WO_4$:$Eu^{3+}$ - a new promising red phosphor. J Non-Cryst Solids 2010;350:1902–7.
[5] Sczancoski JC, Bomio MDR, Cavalcante LS, Joya MR, et al. Morphology and blue photoluminescence emission of $PbMoO_4$ processed in conventional hydrothermal. J Phys Chem C 2009;113:5812–22.
[6] Longo VM, Cavalcante LS, Paris EC, Sczancoski JC, et al. Hierarchical assembly of $CaMoO_4$ nano-octahedrons and their photoluminescence properties. J Phys Chem C 2011;115:5207–19.
[7] Sczancoski JC, Cavalcante LS, Joya MR, Varela JA, et al. $SrMoO_4$ powders processed in microwave-hydrothermal: synthesis, characterization and optical properties. Chem Eng J 2008;140:632–7.
[8] Cavalcante LS, Longo VM, Sczancoski JC, Alemeida MAP, et al. Electronic structure, growth mechanism and photoluminescence of $CaWO_4$ crystals. CrystEngComm 2012;14:853–68.
[9] Boulon G. Fifty years of advances in solid-state laser materials. Opt Mater 2012;34:499–512.
[10] Guzik M, Tomaszewicz E, Guyot Y, Legendziewicz J, et al. Structural and spectroscopic characterizations of two promising Nd-doped monoclinic or tetragonal laser tungstates. J Mat Chem 2012;22:14896–906.
[11] Rushbrooke JG, Ansorge RE. Optical fibre readout and performance of small scintillating crystals for a fine-grained gamma detector. Nucl Instrum Methods 1989;280:83–90.
[12] Guo J, Randall CA, Zhang G, Zhou D, et al. Synthesis, structure, and characterization of new low-firing microwave dielectric ceramics: $(Ca_{1-3x}Bi_{2x}\Phi_x)MoO_4$. J Mat Chem C 2014;2:7364–72.
[13] Xi H, Zhou D, He B, Xie H. Microwave dielectric properties of scheelite structured $PbMoO_4$ ceramic with ultralow sintering temperature. J Am Ceram Soc 2014;97:375–1378.
[14] Vidya S, Solomon S, Thomas JK. Synthesis, characterization, and low temperature sintering of nanostructured $BaWO_4$ for optical and LTCC applications. Adv Cond Mater Phys 2013. https://doi.org/10.1155/2013/409620. article ID 409620.
[15] Kim ES, Kim SH, Lee BI. Low-temperature sintering and microwave dielectric properties of $CaWO_4$ ceramics for LTCC applications. J Eur Ceram Soc 2006;26:2101–4.
[16] Ghosh SK, Rout SK, Tiwari A, Yadav P, et al. Structural refinement, Raman spectroscopy, optical and electrical properties of $(Ba_{1-x}Sr_x)MoO_4$ ceramics. J Mater Sci 2015;26:8319–35.
[17] Tomaszewicz E, Piątkowska M, Pawlikowska M, Groń T, et al. New vacancied and Dy^{3+}-doped molybdates – their structure, thermal stability, electrical and magnetic properties. Ceram Int 2016;42:18357–67.
[18] Bazarganipour M. Synthesis and characterization of $BaMoO_4$ nanostructures prepared via a simple sonochemical method and their degradation ability of

methylene blue. Ceram Int 2016;42:12617–22.
[19] Alencar LDS, Mesquita A, Feitosa CAC, Balzer R, et al. Preparation, characterization and catalytic application of barium molybdate ($BaMoO_4$) and barium tungstate ($BaWO_4$) in the gas-phase oxidation of toluene. Ceram Int 2017;43:4462–9.
[20] Zhang H, Niu ChG, Wen XJ, Wang V, et al. Enhanced visible light photocatalytic activity of $CdMoO_4$ microspheres modified with AgI nanoparticles. Catal Commun 2016;86:124–8.
[21] Golestaneh M. Degradation of organic pollutant in waste water via $CdMoO_4$ nanostructures as an effective photocatalyst; ultrasound-assisted preparation and characterization. J Nanostruct 2019;9:623–9.
[22] Eghbali-Arani M, Pourmasoud S, Ahmadi F, Rahimi-Nasrabadi M, et al. Optimization and detailed stability study on coupling of $CdMoO_4$ into $BaWO_4$ for enhanced photodegradation and removal of organic contaminant. Arab J Chem 2020;13:2425–38.
[23] Kobayashi M, Usuki Y, Ishii M, Senguttuvan N, et al. Significant improvement of $PbWO_4$ scintillating crystals by doping with trivalent ions. Nucl Instrum Methods Phys Res A 1999;434:412–23.
[24] Mikhailik VB, Henry S, Kraus H, Solskii I. Temperature dependence of $CaMoO_4$ scintillation properties. Nucl Instrum Methods Phys Res A 2007;583:350–5.
[25] Belogurov S, Kornoukhov V, Annenkov A, Borisevich A, et al. $CaMoO_4$ scintillation crystal for the search of ^{100}Mo double beta decay. IEEE Trans Nucl Sci 2005;52:1131.
[26] Ishii M, Harada K, KobayashiM, Usuki Y, et al. Mechanical properties of $PbWO_4$ scintillating crystals. Nucl Instrum Methods Phys Res A 1996;376:203–7.
[27] Annenkov AN, Auffray E, Chipaux R, GYu Drobychev, et al. Systematic study of the short-term instability of $PbWO_4$ scintillator parameters under irradiation. Radiat Meas 1998;29:27–38.
[28] Kobayashi M, Usuki Y, Ishii M, Itoh M. Significant increase in fast scintillation component from $PbWO_4$ by annealing. Nucl Instrum Methods Phys Res A 2005;537:312–6.
[29] Guzik M, Tomaszewicz E, Guyot Y, Legendziewicz J, et al. Eu^{3+} luminescence from different sites in scheelite-type cadmium molybdate red phosphor with vacancies. J Mat Chem C 2015;3:8582–94.
[30] Guzik M, Tomaszewicz E, Guyot Y, Legendziewicz J, et al. Structural and spectroscopic characterizations of new vacancied $Cd_{1-3x}Nd_{2x}\square_xMoO_4$ scheelite-type molybdates as potential optical materials. J Mater Chem C 2015;3:4057–69.
[31] Guzik M, Tomaszewicz E, Guyot Y, Legendziewicz J, et al. Spectroscopic properties, concentration quenching and Yb^{3+} site occupations in a vacancied scheelite-type molybdates. J Lumin 2016;169:755–64.
[32] Zhang Z, Sun L, Devakumar B, Liang J, et al. Novel highly luminescent double-perovskite $Ca_2GdSbO_6:Eu^{3+}$ red phosphors with high color purity for white LEDs: synthesis, crystal structure, and photoluminescence properties. J Lumin 2020;221. 117105.
[33] Niu J, Nathan S, Zhang Z, Zhou W. Synthesis and luminescence properties of new red-emitting phosphors $YGe_{0.5}M_{0.5}O_4:Eu^{3+}$ (M = Mo, W). J Lumin 2020;217. 116819.
[34] Han L, Zhang Q, Song J, Xiao Z, et al. A novel Eu^{3+}-doped phosphate glass for reddish orange emission: preparation, structure and fluorescence properties. J Lumin 2020;221. 117041.
[35] Annadurai G, Li B, Devakumar B, Guo H, et al. Synthesis, structural and photoluminescence properties of novel orange-red emitting $Ba_3Y_2B_6O_{15}:Eu^{3+}$ phosphors. J Lumin 2019;208:75–81.
[36] Wang Z, Li JG, Zhu Q, Kim BN, et al. Tartrate promoted hydrothermal growth of highly [001] oriented $(La_{0.95-x}Bi_xEu_{0.05})PO_4$ (x = 0–0.01) nanowires with enhanced photoluminescence. Mater Des 2017;126:115–22.
[37] Daturi M, Busca G, Borel MM, Leclaire A, et al. Vibrational and XRD study of the system $CdWO_4$-$CdMoO_4$. J Phys Chem B 1997;101:4358–69.
[38] Sleight AW, Accurate cell dimensions for ABO_4 molybdates and tungstates. Acta Crystallogr B 972;28:2899-2902.
[39] Liu Y, Jia D, Zhou Y, Zhou Y. Discovery of ABO_4 scheelites with the extra low thermal conductivity through high-throughput calculations. J Materiomics 2020;6:702–11.
[40] Sawicki B, Groń T, Tomaszewicz E, Duda H, et al. Some optical and transport properties of a new subclass of ceramic tungstates and molybdates. Ceram Int 2015;41:13080–9.
[41] Tomaszewicz E, Filipek E, Fuks H, Typek J. Thermal and magnetic properties of new scheelite type $Cd_{1-3x}\square_xGd_{2x}MoO_4$ ceramic materials. J Eur Ceram Soc 2014;34:1511–22.
[42] Groń T, Tomaszewicz E, Berkowski M, Sawicki B, et al. Some optical, magnetic and transport properties of $CdMoO_4:Nd^{3+}$. Ceram Int 2016;42:4185–93.
[43] Groń T, Tomaszewicz E, Berkowski M, Duda H, et al. Dielectric and magnetic properties of $CdMoO_4:Gd^{3+}$ single crystal. J Alloys Compd 2014;593:230–4.
[44] Groń T, Tomaszewicz E, Berkowski M, Oboz M, et al. Magnetic properties of $CdMoO_4:Dy^{3+}$ single crystal. Solid State Phenom 2017;257:107–10.
[45] Uvarov NF, Hairetdinov EF. Temperature dependence of dielectric relaxation in solids. Proc Indian Natn Sci Acad 1989;55A:709–11.
[46] Singh NK, Kumar P, Kumar A, Sharma S. Dielectric relaxation, electrical conductivity and impedance response of Barium titanate (BT) and Strontium titanate (ST) doped $Ba(Fe_{0.5}Nb_{0.5})O_3$ ceramics. J Eng Technol Res 2012;4:104–13.
[47] Bärner K, Zavadskii EA. Coupled soft modes and double triple points in ferroelectrics. Ferroelectrics Lett 1998;24:39–47.
[48] Boultif A, Louër. Powder pattern indexing with the dichotomy method. J Appl Crystallogr 2004;37:724–31.
[49] Agilent CrysAlisPRO. Yarnton, England: Agilent Technologies Ltd; 2015.
[50] Sheldrick GM. Crystal structure refinement with SHELXL. Acta Crystallogr C 2015;71:3–8.
[51] Kaurova IA, Kuz'micheva GM, Brykovskiy AA, Rybakov VB, et al. Influence of growth conditions on structural parameters of scheelite $PbTO_4$ (T = Mo, W) crystals. Mater Des 2016;97:56–63.
[52] Groń T, Tomaszewicz E, Berkowski M, Głowacki M, et al. Yb^{3+}-doped cadmium molybdato-tungstate single crystal – its structural, optical, magnetic and transport properties. J Solid State Chem 2018;262:164–71.
[53] Brese NE, O'Keeffe M. Bond-valence parameters for solids. Acta Crystallogr B 1991;47:192–7.
[54] Brown ID. Recent developments in the methods and applications of the band valence model. Chem Rev 2009;109:6858–919.
[55] Wood RM, Palenik GJ. Bond valance sums in coordination chemistry. A simple method for calculating the oxidation state of cobalt in complex containing only Co-O bonds. Inorg Chem 1998;37:4149–51.
[56] Wood RM, Palenik GJ. Bond valence sums in coordination chemistry. Sodium-oxygen complexes. Inorg Chem 1999;38:3926–30.
[57] Brown ID, Altermatt D. Bond-valence parameters obtained from a systematic analysis of the inorganic crystal structure database. Acta Crystallogr B 1985;41:244–7.
[58] Kubelka P, Munk F. Ein Beitrag zur Optic der Farbanstriche. Z Tech Phys 1931;12:593–601.
[59] Tauc J, Grigorovici R, Vancu A. Optical properties and electronic structures of amorphous germanium. Phys Status Solidi 1966;15:627–37.
[60] Tauc J, Menth A. States in the gap. J Non-Cryst Solids 1972;8–10:569–85.
[61] Viezbicke BD, Patel S, Davis BE, Birnie III DP. Evaluation of the Tauc method for optical absorption edge determination: ZnO thin films as a model system. Phys Status Solidi B 2015;252:1700–10.
[62] Yu T, Wang L, Yang X, Ding W, et al. The luminescence properties and thermal stability of a green-blue color tunable $Sr_2SiO_4:Tb^{3+}$, Ce^{3+} phosphor. Electron Mater Lett 2019;15:18–26.
[63] Das BK, Das T, Parashar K, Parashar SKS, et al. Effect of Cr doping on structural, optical and dielectric properties of ZnO nanoceramics synthesized by mechanical alloying. Electron Mater Lett 2020;16:255–63.
[64] Urbanowicz P, Piątkowska M, Sawicki B, Groń T, et al. Dielectric properties of $RE_2W_2O_9$ (RE = Pr, Sm–Gd) ceramics. J Eur Ceram Soc 2015;35:4181–5.
[65] Wang Q, Li J, Zhang W, Zhong M. Plasma-assisted synthesis of bicrystalline ZnS nanobelts with enhanced photocatalytic ability. Electron Mater Lett 2020;16:180–7.
[66] Arshad M, Abushad M, Husain S, Khan W. Investigation of structural, optical and electrical Transport properties of yttrium doped $La_{0.7}Ca_{0.3}MnO_3$ perovskites. Electron Mater Lett 2020;16:321–31.
[67] Suram SK, Newhouse PF, Gregoire JM. High throughput light absorber discovery, Part 1: an algorithm for automated Tauc analysis. ACS Comb Sci 2016;18:673–81.
[68] Ebraheem S, El-Saied A. Band gap determination from diffuse reflectance measurements of irradiated lead borate glass system doped with TiO_2 by using diffuse reflectance technique. Mater Sci Appl 2013;4:324–9.
[69] Sood K, Singh K, Basu S, Pandey OP. Optical, thermal, electrical and morphological study of $La_{1-x}Ca_xGa_{3-\delta}$ (x = 0, 0.05, 0.10, 0.15 and 0.20) electrolyte. J Eur Ceram Soc 2016;36:3165–71.
[70] Pontes FM, Maurera MAMA, Souza AG, Longo E, et al. Preparation, structural and optical characterization of $BaWO_4$ and $PbWO_4$ thin films prepared by a chemical route. J Eur Ceram Soc 2003;23:3001–7.
[71] Earnshaw A. Introduction to magnetochemistry. London, England: Academic Press; 1968.
[72] Morrish AH. Physical principles of magnetism. New York, USA: John Wiley & Sons, Inc.; 1965.
[73] Kittel C. Introduction to solid state Physics. New York, USA: John Wiley & Sons, Inc.; 1960.
[74] Urbanowicz P, Tomaszewicz E, Groń T, Duda H, Pacyna AW, Mydlarz T. Magnetic properties of R_2WO_6 (where R = Nd, Sm, Eu, Gd, Dy and Ho). Physica B 2009;404:2213–7.
[75] Urbanowicz P, Tomaszewicz E, Groń T, Duda H, Pacyna AW, Mydlarz T, Fuks H, Kaczmarek SM. Influence of Co moment on magnetic properties of $Co_2Sm_2W_3O_{14}$ tungstate. Solid State Phenom 2011;170:1–4.
[76] Urbanowicz P, Tomaszewicz E, Groń T, Duda H, Pacyna AW, Mydlarz T, Fuks H, Kaczmarek SM, Krok-Kowalski J. Superparamagnetic-like behaviour and spin-orbit coupling in $(Co,Zn)RE_4W_3O_{16}$ tungstates (RE = Nd, Sm, Eu, Gd, Dy and Ho). J Phys Chem Solid 2011;72:891–8.
[77] Kalmykov YP, Coffey WT, Crothers DSF, Titov SV. Microscopic models for dielectric relaxation in disordered system. Phys Rev E 2004;70. 041103.
[78] Wübbenhorst M, van Turnhout J. Analysis of complex dielectric spectra. I. One dimensional derivative techniques and three-dimensional modeling. J Non-Cryst Solids 2002;305:40–9.
[79] Sieradzki A, Mączka M, Simenas M, Zaręba JK, et al. On the origin of ferroelectric structural phases in perovskite-like metal–organic formate. J Mater Chem C 2018;6:9420–9.

Bogdan Sawicki was born in 1963. He graduated from the University of Silesia in Katowice (Poland). He obtained his doctoral degree at the Institute of Physics of University of Silesia, where he works until now. He is also involved in IT and computer technology.

Elżbieta Tomaszewicz obtained her PhD in Chemistry from the A. Mickiewicz University (Poznań, Poland) in 2000 and a doctor of sciences degree in Chemistry from the Wrocław University of Science and Technology (Poland) in 2011. She works as an assistant professor at the Department of Inorganic and Analytical Chemistry of West Pomeranian University of Technology in Szczecin (Poland). Her scientific activity is focused on a synthesis and characterization of new RE-doped nano- and micromaterials for laser and LED applications.

Tadeusz Groń was born in 1953. He graduated at the AGH University of Science and Technology (Krakow, Poland) in 1978. He obtained his doctorate in 1989 and a professor of sciences in 2009. He is currently working as a leader research team at the Institute of Physics of University of Silesia (Katowice, Poland). He is the author/co-author of nearly 200 publications as well as announcements presented during national and international conferences.

Marek Berkowski is a professor at the Institute of Physics Polish Academy of Sciences in Warsaw (Poland). His research interests are focused on single crystal growth of advanced materials for optoelectronic applications by different "crucible" methods (Czochralski and Bridgman techniques as well as zonal melting). He has published nearly 300 papers and holds more than 10 patents.

Michał Głowacki received his PhD from the Institute of Physics Polish Academy of Sciences in Warsaw (Poland) under the advisory of Prof. Marek Berkowski. His research activities are focused on design and fabrication of new materials, *i.e.* doped oxide single crystals for optoelectronics.

Monika Oboz graduated from the University of Silesia (Katowice, Poland) in 2005. She defended her PhD in 2009. Now she works at the Institute of Physics of the University of Silesia. Her current scientific interest is mainly on the obtaining single crystals using Czochralski method from a levitation melt and investigations of magnetic properties.

Joachim Kusz is a professor at the University of Silesia in Katowice (Poland). His scientific interests are phase transitions, modulated structures and complex compounds which exhibit spin crossover.

Sebastian Pawlus Dr. Sci., PhD was born in 1976. He obtained his doctorate in Physics in 2004. He is currently working at the Institute of Physics of University of Silesia (Katowice, Poland). His current research involves the use of various experimental techniques, *e.g.* dielectric spectroscopy at different thermodynamic conditions to explore electric and relaxation properties of various solid state and associated liquids.